ORIGINAL PAPER

Benchmark problems for reactive transport modeling of the generation and attenuation of acid rock drainage

K. Ulrich Mayer[1] · Peter Alt-Epping[2] · Diederik Jacques[3] · Bhavna Arora[4] · Carl I. Steefel[4]

Abstract Acid rock drainage (ARD) is a problem of international relevance with substantial environmental and economic implications. Reactive transport modeling has proven a powerful tool for the process-based assessment of metal release and attenuation at ARD sites. Although a variety of models has been used to investigate ARD, a systematic model intercomparison has not been conducted to date. This contribution presents such a model intercomparison involving three synthetic benchmark problems designed to evaluate model results for the most relevant processes at ARD sites. The first benchmark (ARD-B1) focuses on the oxidation of sulfide minerals in an unsaturated tailing impoundment, affected by the ingress of atmospheric oxygen. ARD-B2 extends the first problem to include pH buffering by primary mineral dissolution and secondary mineral precipitation. The third problem (ARD-B3) in addition considers the kinetic and pH-dependent dissolution of silicate minerals under low pH conditions. The set of benchmarks was solved by four reactive transport codes, namely CrunchFlow, Flotran, HP1, and MIN3P. The results comparison focused on spatial profiles of dissolved concentrations, pH and pE, pore gas composition, and mineral assemblages. In addition, results of transient profiles for selected elements and cumulative mass loadings were considered in the intercomparison. Despite substantial differences in model formulations, very good agreement was obtained between the various codes. Residual deviations between the results are analyzed and discussed in terms of their implications for capturing system evolution and long-term mass loading predictions.

Keywords Reactive transport modeling · Model intercomparison · Benchmark · Acid rock drainage

✉ K. Ulrich Mayer
umayer@eos.ubc.ca

1 Department of Earth, Ocean and Atmospheric Sciences, University of British Columbia, 2207 Main Mall, Vancouver, BC V6T 1Z4, Canada

2 Rock-Water Interaction Group, Institute of Geological Sciences, University of Bern, Baltzerstrasse 3, 3012 Bern, Switzerland

3 Belgian Nuclear Research Centre SCK.CEN, Boeretang 200, Mol B-2400, Belgium

4 Earth Sciences Division, Lawrence Berkeley National Laboratory, Berkeley, CA 94720, USA

1 Introduction

The impact of mining on groundwater and surface water poses an important environmental problem of global relevance [9]. Many mine waste deposits contain reactive sulfide minerals, which are unstable when in contact with the atmosphere [9, 26]. The oxidation of these mineral phases leads to the acidification of pore water, which subsequently percolates downward along the natural gradient (Fig. 1). These acidified waters are usually characterized by high Fe and SO_4 concentrations and can potentially carry a suite of toxic metals including Cu, Pb, Zn, and other trace metals. Acid rock drainage is typically generated in mine waste deposits including tailings and waste rock piles, but also in abandoned mine workings [9, 26].

There is the potential for migration of dissolved metals away from a mine waste disposal area, causing the degradation of groundwater and surface water resources. This can lead to a perturbation of natural environments, threatening flora and fauna, in particular aquatic life. To avoid environmental impact, treatment of the drainage water is necessary, often for time periods of decades or even centuries [9]. The associated
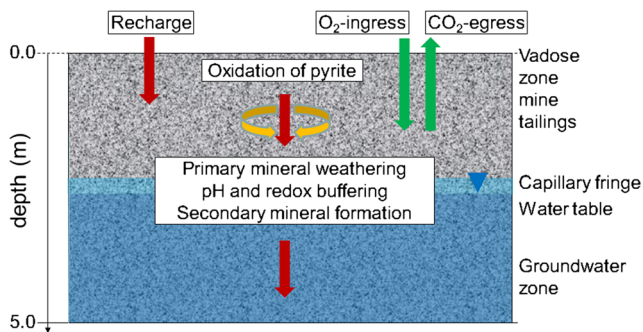
Fig. 1 Conceptual model of ARD generation and attenuation

cost of acid rock drainage (ARD) remediation and management at abandoned and orphaned mines in North America alone has been estimated in the tens of billions of US dollars [9]. As a result, projections of ARD generation, release, and treatment requirements need to be taken into consideration at the design stage of a mine. A thorough process understanding is paramount to advance the predictive capabilities for assessing future ARD generation.

Reactive transport modeling has proven a useful tool to assess processes of water-rock interaction and has been applied extensively to investigate the complex interactions during ARD generation and attenuation. The application of reactive transport models to assess metal leaching at mine sites was introduced through the pioneering work of Cathles [6] and Jaynes et al. [11]. In the following years, a number of studies were conducted to evaluate the attenuation of metals in fully saturated mine tailings [e.g., 32, 33]. The simulation of metal release also required the consideration of vadose zone flow and transport processes, including gas transport, which was the subject of a number of follow-up studies [1, 15, 19, 22, 34, 35]. More recently, reactive transport modeling has also been applied to investigate the release and attenuation of metals in waste rock piles [13, 17, 22]. Models have been used to investigate ARD generation and fate at both the laboratory [e.g., 8] and the field scale [13, 22]. Although the components of these models have been tested and verified, a direct model intercomparison for a problem involving the generation and attenuation of ARD has not been published to date.

The objective of this contribution is to provide a benchmark that focuses on the most important processes controlling drainage water evolution at ARD sites and to determine whether existing reactive transport codes arrive at the same solution, when solving these problems. To this extent, three hypothetical scenarios were devised to evaluate formulations and compare implementations for simulating the oxidation of sulfide minerals and the attenuation of ARD in partially saturated mine waste. Processes considered in this benchmark include variably saturated flow, multicomponent solute transport, diffusion of oxygen and carbon dioxide in the gas phase, sulfide mineral oxidation,

the dissolution of gangue minerals, and precipitation and re-dissolution of secondary mineral phases. The benchmark is restricted to one-dimensional simulations in partially saturated media under steady-state flow conditions. The evaluation of additional processes such as gas advection, gas convection, and preferential flow, which can also be of importance—in particular in waste rock, are beyond the scope of this paper. Four different reactive transport codes participated in this model intercomparison exercise, namely CrunchFlow [29], Flotran [16], HP1 [10], and MIN3P [19, 20].

2 Governing equations

A detailed description of the formulation of multicomponent reactive transport models is provided in Steefel et al. [29]. However, to provide context for the current simulations, the subset of the governing equations relevant to the present benchmark is provided here.

2.1 Variably saturated flow

Variably saturated flow is solved by Richards equation [25, 27] under the assumption of a passive air phase and neglecting hysteresis:

$$S_a S_s \frac{\partial h}{\partial t} + \phi \frac{\partial S_a}{\partial t} - \nabla \cdot [k_{ra} \mathbf{K} \nabla h] - Q_a = 0, \qquad (1)$$

where S_a [m^3 H$_2$O m^{-3} void] defines the saturation of the aqueous phase, S_s [m^{-1}] is the specific storage coefficient, h [m] is hydraulic head, t [s] is time, ϕ [m^{-3} void m^{-3} porous medium] is porosity, k_{ra} [−] is the relative permeability, K [ms^{-1}] is the hydraulic conductivity tensor, and Q_a is a source-sink term [m^3 H$_2$O m^{-3} porous medium s^{-1}]. The relative permeability and aqueous phase saturation are calculated using the soil hydraulic functions given by van Genuchten [30]:

$$S_a = S_{ra} + \frac{1 - S_{ra}}{\left(1 + \alpha \psi_a^n\right)^m} \qquad (2)$$

$$k_{ra} = S_{ea}^l \left[1 - \left(1 - S_{ea}^{1/m}\right)^m \right]^2 \qquad (3)$$

$$S_{ea} = \frac{S_a - S_{ra}}{1 - S_{ra}} \qquad (4)$$

where S_{ra} [−] defines the residual saturation of the aqueous phase; ψ_a is the pressure head [m]; α [m^{-1}], n, m, and l are soil hydraulic function parameters, with $m = 1 - 1/n$. S_{ea} is the effective saturation of the aqueous phase.

2.2 Multicomponent reactive transport

The equations for reactive transport of N_c dissolved components, accounting for advective-dispersive solute transport and diffusive gas transport, are defined by [e.g., 19]:

$$
\begin{aligned}
& \frac{\partial}{\partial t}\left[S_a \phi T_j^a\right] + \frac{\partial}{\partial t}\left[S_g \phi T_j^g\right] \\
& \quad + \nabla \cdot \left[\mathbf{q}_a T_j^a\right] - \nabla \cdot \left[S_a \phi \mathbf{D}_a \nabla T_j^a\right] \\
& \quad - \nabla \cdot \left[S_g \phi \mathbf{D}_g \nabla T_j^g\right] \\
& \quad - Q_j^{a,m} = 0 \qquad j = 1, N_c
\end{aligned}
\tag{5}
$$

where T_j^a [mol L^{-1} H$_2$O] is the total aqueous component concentration, T_j^g [mol L^{-1} gas] is the total component concentration of the gaseous species, S_g is the saturation of the gas phase, q_a is the Darcy flux vector, which can be obtained from the solution of Eq. (1), D_a is the hydrodynamic dispersion tensor applicable to all species dissolved in the system, and D_g is the pore gas diffusion tensor applicable to all gases. $Q_j^{a,m}$ are source-sink terms [mol dm^{-3} porous medium s^{-1}] due to kinetically controlled mineral dissolution-precipitation reactions. The pore gas phase diffusion coefficient is defined locally based on porosity and saturation following the relationship given by Millington [23]:

$$
D_g = \phi^{1/3} S_g^{7/3} D_g^0
\tag{6}
$$

where D_g^0 is the free phase diffusion coefficient in the gas phase, assumed to be equivalent for all gases. The same formulation is used to determine aqueous phase diffusion coefficients.

Advective gas transport or multicomponent gas diffusion is not included in the current benchmark. Although these transport processes were previously implemented by Binning et al. [4] and Molins et al. [21], other codes participating in this benchmark do not possess this capability. Similarly, the model by Binning et al. [4] does not include the necessary geochemical simulation capabilities. It was therefore not possible to consider advection and multicomponent gas diffusion as part of this exercise. The impact of this simplification is limited, considering that the maximum difference of the oxygen gas fluxes as a function of the model formulation is approximately 20 % with increased gas ingress by advection induced by oxygen consumption as a result of pyrite oxidation [4, 21]. In many cases, the difference is less, because CO$_2$ is generated as a result of carbonate mineral dissolution counteracting the buildup of an inward pressure gradient [21].

In addition to maintaining the mass balance for aqueous and gaseous species (provided by Eq. (5)), it is necessary to provide a mass balance equation for the mineral phases:

$$
\frac{d\varphi_i}{dt} = V_i^m R_i^m \qquad i = 1, N_m
\tag{7}
$$

where φ_i [−] is the volume fraction of the mineral in question, V_i^m [dm^3 mineral mol^{-1}] is the molar volume, and R_i^m [mol dm^{-3} porous medium s^{-1}] is the rate of mineral dissolution-precipitation; N_m is the number of minerals considered.

The current benchmark set includes a suite of geochemical reactions that can be described by the following set of stoichiometric relationships:

$$
A_i^a \leftrightarrow \sum_{j=1}^{N_c} \nu_{ij}^a \; A_j^c \quad i = 1, N_a
\tag{8}
$$

$$
A_i^g \leftrightarrow \sum_{j=1}^{N_c} \nu_{ij}^g \; A_j^c \quad i = 1, N_g
\tag{9}
$$

$$
A_i^m \leftrightarrow \sum_{l=1}^{N_i^{m,p}} \sum_{j=1}^{N_c} \nu_{ijl}^m \; A_j^c \qquad i = 1, N_m
\tag{10}
$$

Here, A_i^a, A_i^g, and A_i^m are the names of the aqueous complexes, gases, and minerals, respectively, and ν_{ij}^a, ν_{ij}^g, ν_{ijl}^m define the stoichiometric coefficients of the components A_j^c, which constitute the N_c primary unknowns present in the aqueous phase. N_a and N_g define the number of aqueous complexes and gases; $N_i^{m,p}$ define the number of parallel pathways affecting the kinetic dissolution or precipitation of mineral A_i^m. Equation (8) is also used to compute concentrations of redox couples at equilibrium.

This reaction network includes both equilibrium reactions (Eqs. (8) and (9)) and kinetically controlled reactions (Eq. (10)). All equilibrium relationships enter the reactive transport Eq. (5) through component mass balances defined by total concentration terms, while kinetic reactions are considered through source-sink terms.

The total component concentrations T_j^a in the aqueous phase are defined as [28, 31]

$$
T_j^a = C_j^c + \sum_{i=1}^{N_a} \nu_{ij}^a C_i^a \qquad j = 1, N_c,
\tag{11}
$$

where C_j^c are the concentrations of the components as species in solution [mol L^{-1} H$_2$O] and C_i^a are the concentrations of secondary species in the aqueous phase [mol L^{-1} H$_2$O]. The total component concentrations in the gas phase are given by

$$
T_j^g = \sum_{i=1}^{N_g} \nu_{ij}^g C_i^g, \qquad j = 1, N_c
\tag{12}
$$

where C_i^g is the concentration of the gas A_i^g [mol L^{-1} gas]. The concentrations of secondary species (e.g., C_i^a, C_i^g) are

determined based on law of mass action relationships subject to the appropriate activity corrections [e.g., 29]. Activity corrections considered in this benchmark are based on the extended Debye-Hückel equation following the formulation implemented in MINTEQA2 [2]. Debye-Hückel parameters are provided in the Supplementary Material.

Kinetic reactions lead to the mass transfer between minerals and the aqueous phase. The release or uptake of aqueous components due to dissolution-precipitation reactions is given by

$$Q_j^{a,m} = -\phi \sum_{i=1}^{N_m} \sum_{l=1}^{N_i^{m,p}} \nu_{ijl}^m R_{il}^m \qquad j = 1, N_c \qquad (13)$$

where R_{il}^m is the rate of dissolution or precipitation of the mineral A_i^m along the lth reaction pathway.

Unless otherwise noted, mineral dissolution-precipitation reactions are described as kinetically controlled reactions based on the simple rate expression [12]:

$$R_i^m = -k_i^m \left[1 - \left(\frac{IAP_i^m}{k_i^m} \right) \right] \qquad (14)$$

where R_i^m is the reaction rate, IAP_i^m is the ion activity product, K_i^m is the equilibrium constant for the reaction and k_i^m is the effective rate constant. For primary mineral phases, a two-third power relationship of the form

$$k_i^{m,t} = -k_i^{m,o} \left(\frac{\varphi_i^t}{\varphi_i^o} \right)^{2/3} \qquad (15)$$

is used to update the effective rate constant [14]. In this relationship, k_i^t and φ_i^t define the effective rate constant and mineral volume fraction, respectively, while k_i^0 and φ_i^0 define the initial rate constant and mineral volume fraction, respectively.

3 Definition of benchmark problems

The present benchmark is subdivided into three levels with increasing complexity (Table 1)—the first benchmark (ARD-B1) focuses on the ingress of atmospheric oxygen through the gas phase of a partially saturated tailing impoundment resulting in the oxidation of pyrite, acid generation, and the

Table 1 Overview of the acid rock drainage benchmarks

Level	Description
ARD-B1	Pyrite oxidation in mine tailings
ARD-B2	Pyrite oxidation, pH buffering by carbonate and hydroxide minerals, and secondary mineral formation
ARD-B3	Pyrite oxidation, pH buffering by carbonate, hydroxide, and silicate minerals, secondary mineral formation

release of Fe and SO_4. The second benchmark level (ARD-B2) builds on the first level and adds complexity by considering dissolution and precipitation of carbonate, hydroxide, and sulfate minerals, resulting in pH buffering and metal attenuation. The third benchmark level (ARD-B3) further increases the complexity by introducing the irreversible weathering of silicate mineral phases. Although additional processes may play a role in the weathering of tailings impoundments, e.g., spatial complexity [36], energy balances [1], and phenomena such as atmospheric pumping [3] and microbially mediated processes [36], it is most practical to focus this benchmark on the most relevant processes controlling ARD generation and attenuation. This approach allows the participation of a larger number of codes and provides a baseline code intercomparison for ARD studies. In the following, parameters that are common to all three benchmark levels are described first, followed by the parameters that are specific to each benchmark level. All benchmark parameters are loosely based on previous simulations of ARD generation and attenuation in actual tailings impoundments [18, 19] and can be considered typical for sulfidic tailings with low carbonate content under temperate climate conditions. Common to all benchmarks are the spatial domain, discretization, as well as physical parameters for flow and transport.

3.1 Spatial and temporal discretization

All three benchmark levels consider a partially saturated, vertical one-dimensional model domain 5.0 m in length with a cross-sectional area of 1 m^2. The domain is uniformly discretized into 101 control volumes including two boundary control volumes (the first and the last control volumes of the grid are half size of the regular control volumes to ensure that the grid cells are located on the boundary of the domain). Effectively, the spatial discretization is 0.05 m and the final simulation time is 10 years. The complexity of the benchmark problem with multiple dissolution-precipitation fronts, phase disappearance, and steep geochemical gradients does not allow the specification of a code-independent time stepping scheme. As a result, time discretization was not specified and was chosen by each participating group independently.

3.2 Flow model specification

The benchmark problems involve partially saturated steady state flow with a saturated hydraulic conductivity of 1.0×10^{-6} m s^{-1}, chosen to represent a value typical for mine tailings. Table 2 summarizes all flow input parameters including the soil hydraulic function parameters required for parameterization of Eqs. (2)–(4). A specified flux boundary is used at the top of the column (q=9.51×10^{-9} m s^{-1}, corresponding to 300 mm year^{-1}) to simulate annual recharge. A constant head (first type) boundary condition is assigned at the outflow end

Table 2 Flow parameters for the model domain

Parameter	Unit	Value
Hydraulic conductivity	m s^{-1}	1.0×10^{-6}
Residual saturation	–	0.05
van Genuchten alpha	m^{-1}	3.5
van Genuchten n	–	1.4
van Genuchten l	–	0.5
Air entry pressure	m	0.0

of the column (h=2.5 m). Resulting water and gas saturations versus depth provide the foundation for the reactive transport intercomparison and are presented in Fig. 2. Based on these specifications, the water table is located in the center of the domain (indicated by an inverted triangle, Fig. 2), which allows testing of code performance for conditions including the transition from unsaturated to fully saturated conditions. The solution of the flow problem is not necessary to run this benchmark, and alternatively, the water and gas saturations and the steady state water flux can be used as input for the reactive transport problems (provided in the Supplementary Material).

3.3 Transport model specification

All transport parameters including porosity, aqueous, and gaseous free phase diffusion coefficients and longitudinal dispersivity of the medium are summarized in Table 3. A mixed boundary condition is applied at the inflow boundary (for concentrations see Supplementary Material: Table S.1 for the benchmark levels ARD-B1–ARD-B3), while a free

Fig. 2 Steady-state water and gas saturations along vertical profile (MIN3P results)

Table 3 Transport parameters for the model domain

Parameter	Unit	Value
Porosity	–	0.5
Free phase diffusion coefficient in water	m^2 s^{-1}	2.4×10^{-9}
Free phase diffusion coefficient in soil gas	m^2 s^{-1}	2.1×10^{-5}
Longitudinal dispersivity	m	5.0×10^{-4}

exit boundary condition (advection only) is applied at the outflow boundary. The mixed type boundary condition is a third type boundary condition for all aqueous components (specified flux). However, influx and outflux of O_2 and CO_2, respectively, are also allowed through the gas phase. This is achieved by extending the grid by an additional cell (or a ghost cell) into an atmospheric boundary layer, where atmospheric gas composition is assumed as fixed (i.e., first type boundary condition for $O_2(g)$ and $CO_2(g)$).

3.4 Geochemical reaction network and initial conditions

3.4.1 Benchmark ARD-B1

The first benchmark (ARD-B1) considers the ingress of atmospheric oxygen into the partially saturated solution domain, leading to the oxidation of pyrite, a decrease of pH and downward transport of Fe and SO_4. Processes considered are advective-dispersive solute transport, diffusive gas transport, kinetically controlled oxidative mineral dissolution, aqueous complexation, redox equilibrium, and gas exchange reactions.

The only mineral phase considered is pyrite at a volume fraction of 2×10^{-3} [m^3 m^{-3}], the remaining fraction of the solid phase is assumed inert. The oxidative dissolution of pyrite is described by a kinetically surface-controlled reaction (Eq. (14)) with an initial dissolution rate constant of 3×10^{-10} mol dm^{-3} bulk s^{-1}, and the rate constant is updated using the two-third power relationship described above (Eq. (15)).

In addition to H_2O, 10 aqueous components are included already at this level to allow for straightforward extension to the higher levels of the benchmark set. These components are $O_2(aq)$, Al^{3+}, CO_3^{2-}, Ca^{2+}, Cl^-, Fe^{2+}, H^+, K^+, SO_4^{2-}, and H_4SiO_4 and form 21 aqueous complexes. The components Fe^{2+} and SO_4^{2-} are redox active, defined by the Fe^{2+}/Fe^{3+} and SO_4^{2-}/HS^- redox couples. Equilibrium partitioning of O_2 and CO_2 between the gas phase and the water phase is assumed. Initial conditions for the aqueous phase are provided in Table S.1 (Supplementary Material). All geochemical reactions and associated thermodynamic and kinetic data for the aqueous components, complexed aqueous species, minerals, gas exchange reactions, and redox equilibrium reactions are provided in the Supplementary Material (Tables S.3 – S.8).
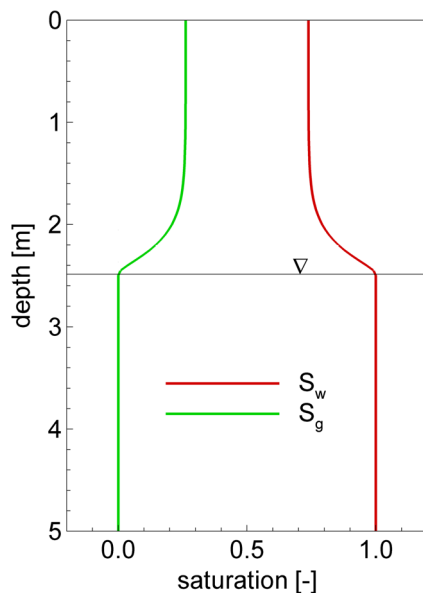
3.4.2 Benchmark ARD-B2

The second benchmark (ARD-B2) builds on the first benchmark level by adding several primary and secondary mineral phases. This benchmark was designed to evaluate the ability of the codes to simulate acid neutralization processes induced by reactive mineral phases, such as carbonates and hydroxides. In addition to pyrite, calcite and gibbsite are considered as primary phases, present at small volume fractions (Supplementary Material, Table S.2). In addition, ferrihydrite, jarosite, and gypsum are considered as potential secondary mineral phases. Initial rate constants for all primary and secondary phases (except pyrite) are set to 1×10^{-8} mol dm^{-3} bulk s^{-1}, implying near equilibrium conditions for the dissolution and precipitation of these minerals. The initial conditions for the aqueous phase are detailed in Table S.1 (Supplementary Ma-

terial). Thermodynamic and kinetic parameters are provided in Tables S.4–S.8, Supplementary Material.

3.4.3 Benchmark ARD-B3

The third benchmark (ARD-B3) builds on the second level and adds irreversible dissolution of the silicate mineral phases K-feldspar and muscovite and the precipitation of secondary amorphous silica. This benchmark is designed to provide an opportunity to compare reactive transport codes for a problem involving both fast and slow acid neutralization reactions.

The kinetic irreversible dissolution of K-feldspar and muscovite are described by the following rate expressions, each involving parallel pH-dependent reaction pathways for acidic and basic pH conditions (K-feldspar: [5], muscovite: [24]):

$$
\text{K-feldspar}: R_{\text{k-feldsp}}^{\text{m}} = -\max\left[A_{\text{k-feldsp}} \left[10^{-9.93}\{H^+\}^{0.5} + 10^{-16.5}\{H^+\}^{-0.45} \right] \left(1 - \frac{IAP_{\text{k-feldsp}}}{K_{\text{k-feldsp}}^{\text{m}}} \right), 0 \right] \tag{16}
$$

$$
\text{Muscovite}: R_{\text{musc}}^{\text{m}} = -\max\left[A_{\text{musc}} \left[10^{-12.6}\{H^+\}^{0.08} + 10^{-13.5}\{H^+\}^{-0.10} \right] \left(1 - \frac{IAP_{\text{musc}}}{K_{\text{musc}}^{\text{m}}} \right), 0 \right] \tag{17}
$$

with reactive surface areas of $A_{\text{k-feldsp}} = 10$ m^2 dm^{-3} bulk and $A_{\text{musc}} = 30$ m^2 dm^{-3} bulk. The dependencies on H$^+$ are in terms of activities, not concentrations. Initial volume fractions for all primary phases are provided in Table S.2, while the initial condition for the aqueous phase is provided in Table S.1 (Supplementary Material).

4 Participating reactive transport codes

Four reactive transport codes participated in this benchmark intercomparison exercise: CrunchFlow [29], Flotran [16], HP1 [10], and MIN3P [19]. Crunchflow, Flotran, and MIN3P use the global implicit method (GIM), while the formulation of HP1 is based on an operator splitting method, implemented as the sequential non-iterative approach (SNIA) by coupling HYDRUS1D to PHREEQC [10]. A more detailed description of the formulation and capabilities of the participating codes can be found in Steefel at al. [29], including a table that provides a comprehensive side-by-side comparison of the code features. Input and database files, as well as selected output

files for the four participating codes CrunchFlow, Flotran, HP1 and MIN3P are provided as either text files or excel files in the Supplementary Material.

5 Results and discussion

5.1 Benchmark ARD-B1

Simulation results for the benchmark ARD-B1 (T=10 years, corresponding to 1.4 pore volumes of water displacement) show the oxidative dissolution of pyrite in the upper section of the model domain combined with a gradual depletion of O$_2$. Fe and SO$_4$ are released and pH declines to values below 2 along the flowpath. A drastic change in redox state is simulated in the region where O$_2$ becomes depleted, leading to a sharp decline in pE (Fig. 3). This behavior is the result of assuming redox equilibrium for the Fe(III)/Fe(II) and SO$_4$/ HS$^-$ redox couples. At the redoxcline, there are also drastic changes in Fe(II) and Fe(III) concentrations, as dissolved Fe(III) is converted to Fe(II), leading to sharp gradients in this region.

Fig. 3 Simulated profiles after 10 years for benchmark ARD-B1: **a** pH and pE; **b** pyrite volume fraction; **c** total aqueous component concentrations of Fe(II), Fe(III), and SO$_4$; **d** pO$_2$— *solid lines*: MIN3P, *dashed lines*: HP1, *dot-dashed lines*: Flotran, *dotted lines*: CrunchFlow
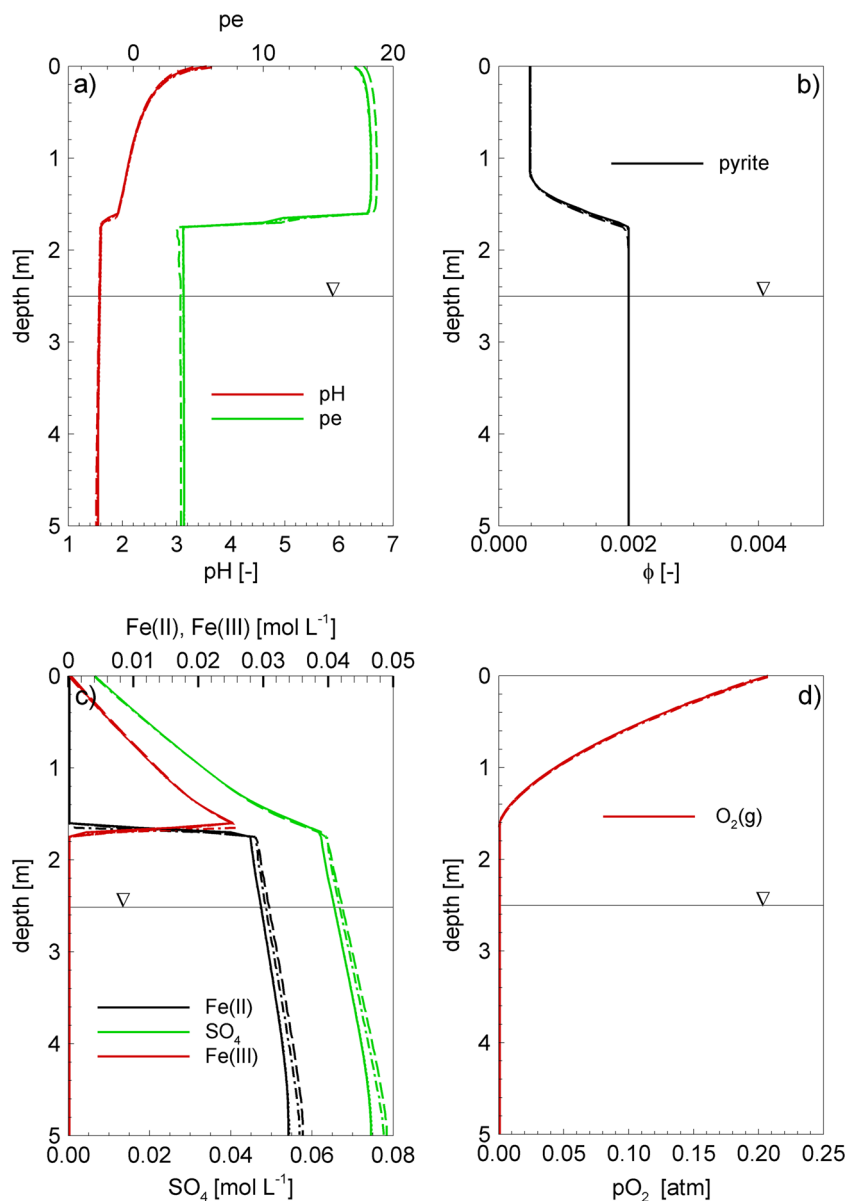

As can be seen from Fig. 3, there is excellent agreement between all participating codes for pH, pyrite volume fractions, and pO$_2$. Slight differences can be observed for pE; however, these differences are not significant and can likely be attributed to the various implementations of redox processes in the different codes. Some more significant discrepancies can be observed for dissolved Fe(II) and SO$_4$ concentrations at the base of the domain (Fig. 3c), showing different concentrations exiting the domain after 10 years of simulation time. To investigate this divergence of results further, Fig. 4 shows a comparison of the breakthrough curves for Fe(II) and SO$_4$ at the base of the domain. These results indicate a near perfect agreement between CrunchFlow and MIN3P (results cannot be distinguished visually), while the solution for Flotran and HP1

show small deviations. It is difficult to pinpoint the exact cause for these differences, as they may be related to several reasons including variations in the implementation of the transport scheme, time stepping, small deviations in the database due to the use of different components, the coupling scheme between transport and reactions, and the implementation of the model for activity corrections.

A sensitivity analysis on the effect of time stepping was conducted with the MIN3P code. The maximum time step was varied by two orders of magnitude; however, the effect on the results was insignificant (not visible in direct comparison plots). A comprehensive sensitivity analysis involving all codes may be helpful in revealing the source of the remaining differences; however, such an exercise is beyond the scope of the current contribution. Overall, the breakthrough curves
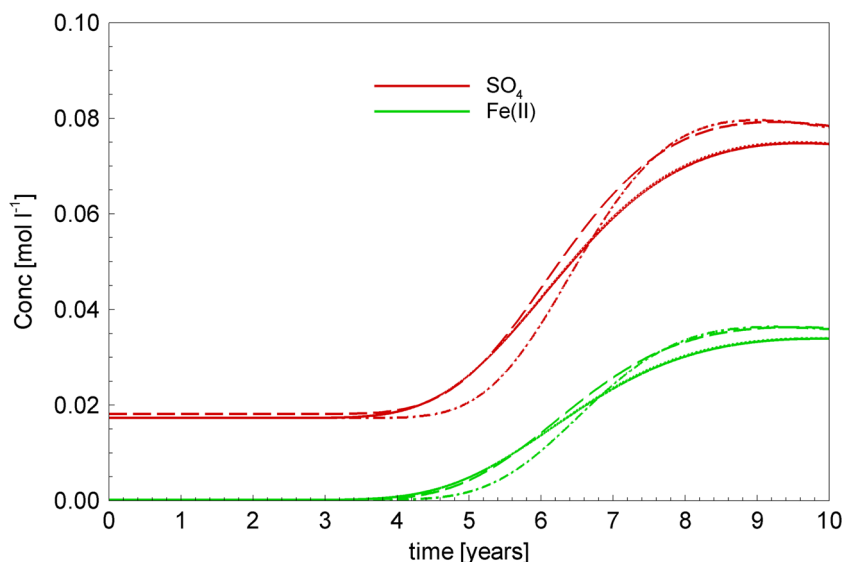
indicate that the transient evolution of the system is consistently described by all four participating codes, showing the arrival of elevated Fe(II) and SO_4 concentrations between 4 and 8 years of simulation time.

One of the key criteria for simulation of acid rock drainage is the capability of the codes to provide cumulative measures for sulfide oxidation and elemental release at discharge points. This capability is required to assess the long-term evolution of waste deposits and to provide an estimate of water treatment requirements. Although the current benchmark is hypothetical in nature, it provides an opportunity to verify the implementation of the governing equations outlined above with respect to the cumulative mass balance. To assess agreement between the codes, Table 4 compares the total oxygen uptake across the top of the tailings (as a measure of cumulative sulfide oxidation) and the total Fe(II) and SO_4 release at the base of the solution domain (after $T=10$ years). Excellent agreement was obtained between the results of CrunchFlow and MIN3P (differences are <1 % for all parameters) and results for Flotran are also in close agreement. Results by HP1 are slightly higher for oxygen ingress (<1 %), as well as Fe(II) and SO_4 release (appr. 5 %). Although the reason for this difference cannot be identified with certainty, it may be due to the use of the SNIA in HP1, introducing small operator splitting errors.

A closer look at the system mass balance also reveals one of the key difficulties of this benchmark. Although only 1.4

pore volumes of water are displaced during the 10-year simulation period, substantial turnover occurs for gas phase O_2. The total O_2 content in the gas phase at $T=10$ years is 0.69 mol (based on MIN3P model results). Normalizing the total O_2 ingress (Table 4) to this O_2 content reveals the ingress and consumption of approximately 500 pore volumes of gas phase O_2 over the simulation period.

5.2 Benchmark ARD-B2

Simulation results for the benchmark ARD-B2 also show the oxidative dissolution of pyrite in the upper section of the model domain combined with a gradual depletion of O_2 with depth. Fe and SO_4 are released, but at lower concentrations due to acid neutralization reactions caused by the dissolution of calcite and gibbsite, secondary mineral formation, and re-dissolution. A series of mineral dissolution-precipitation fronts, commonly observed in ARD environments [19, 32], leads to a stepwise increase of pH along the flow path. Calcite dissolution buffers the pH to values slightly above 6, followed by a gibbsite buffer (pH=4), ferrihydrite buffer (pH=3), and the jarosite dominated region near the ground surface (with pH values as low as 2). The simulation also indicates diffusive egress of CO_2 towards the atmosphere above the water table and entrapment of CO_2 below the water table (Fig. 5).

Considering the level of complexity of this benchmark, excellent agreement is reached between all codes for pH, pE, pO_2, and the mineralogical alteration of the tailings (Fig. 5). Although the results show some differences for SO_4 and Fe(II) (Fig. 5c), in particular in the redox transition zone, the cumulative release of SO_4 and Fe(II) at the base of the domain are nearly identical amongst all codes. The most significant differences can be seen at the redoxcline for Fe(II) and Fe(III) and for CO_2(g) in the region of the water table. Differences for Fe(II) and Fe(III) are most pronounced for HP1 and may be due to the use of the

Table 4 Cumulative oxygen ingress, cumulative SO_4 and Fe(II) release after 10 years—benchmark ARD-B1

Mass ingress/release [mol]	CrunchFlow	Flotran	HP1	MIN3P
O_2-ingress	344.0	345.9	349.0	344.1
SO_4-release	116.7	116.4	123.0	116.5
Fe(II)-release	37.3	39.6	39.8	37.2

Fig. 5 Simulated profiles after 10 years for benchmark level II: **a** pH and pE; **b** mineral volume fractions; **c** total aqueous component concentrations of Fe(II), Fe(III), and SO$_4$; **d** pO$_2$ and pCO$_2$—*solid lines*: MIN3P, *dashed lines*: HP1, *dot-dashed lines*: Flotran, *dotted lines*: CrunchFlow
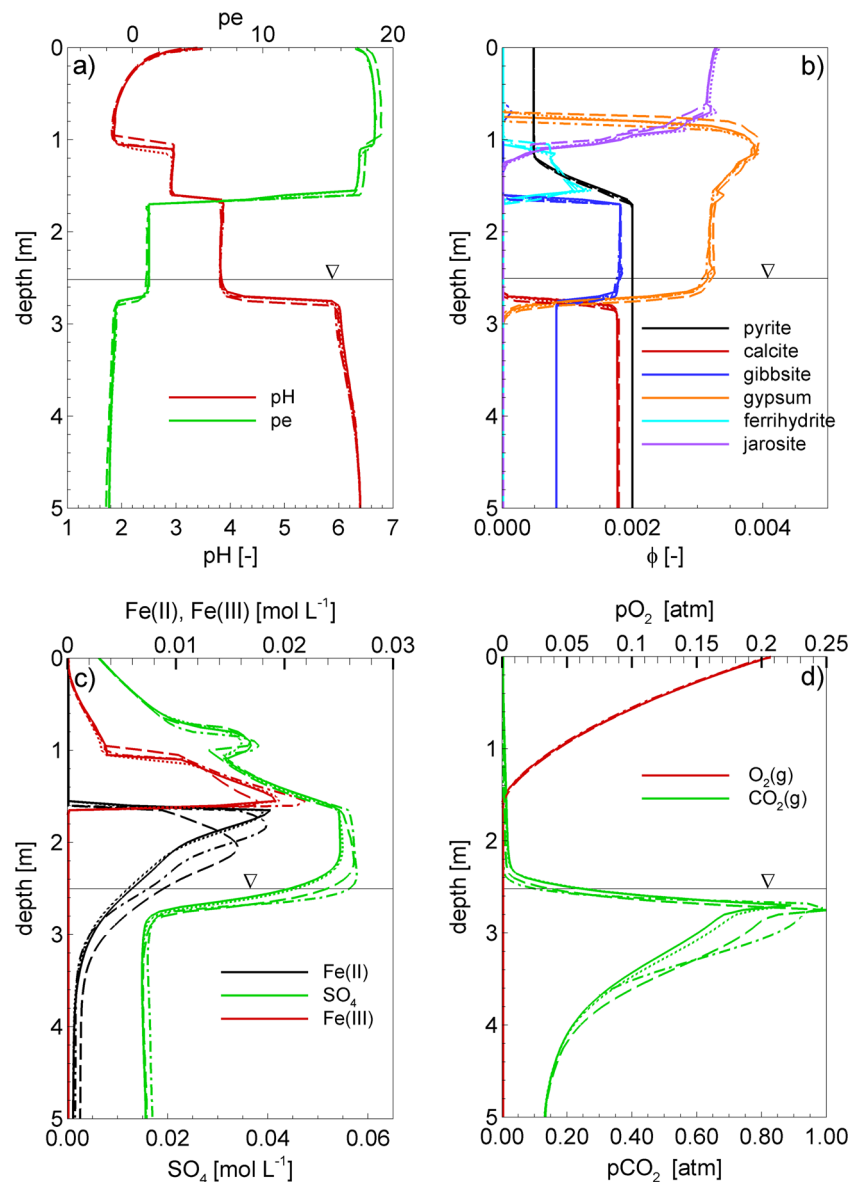
SNIA coupling method and the short characteristic time scale of gas transport. CO$_2$(g) is controlled by the dissolution of calcite in response to acid generation. CO$_2$ is initially released to the atmosphere via diffusion through the gas phase; however, as calcite disappears from the vadose zone, CO$_2$ remains in solution and migrates downwards with the flowing groundwater (Fig. 5d). This transition is strongly dependent on the timing of the complete depletion of calcite near the water table.

Similar to ARD-B1, results of the code intercomparison show a near perfect agreement between CrunchFlow and MIN3P, despite the increased complexity of this benchmark level. Although the results obtained with Flotran and HP1 slightly differ from those obtained by the other two codes, the overall system evolution including the location of mineral dissolution-precipitation fronts and pH buffer zones is nearly identical for all four codes (Fig. 5).

As an additional measure of agreement between the codes, cumulative O$_2$ ingress, CO$_2$ egress, and release of Fe(II) and SO$_4$ are reported in Table 5. Differences between CrunchFlow and MIN3P are again <1 % for all parameters. In general, all codes show very good agreement for O$_2$ ingress, CO$_2$ egress, and SO$_4$ release at the discharge point. Percentage differences for Fe(II), however, seem significant, with cumulative mass releases ranging between 0.8 and 1.6 mol over the 10-year simulation period. Although this difference seems large, it has to be kept in mind that Fe(II) turnover in the solution domain is substantial involving pyrite oxidation as a source. The total Fe(II) release due to pyrite oxidation is close to 100 mol over the simulation period (according to MIN3P mass balance results), implying that only between 0.8 and 1.6 % of Fe(II) exit the solution domain, based on the

Table 5 Cumulative oxygen ingress, cumulative SO$_4$ and Fe(II) release after 10 years—benchmark ARD-B2

Mass ingress/release/egress [mol]	CrunchFlow	Flotran	HP1	MIN3P
O$_2$(g) ingress	346.6	346.1	350.0	343.8
SO$_4$ release	51.3	52.7	53.1	51.4
Fe(II) release	0.8	1.0	1.6	0.8
CO$_2$(g) egress (gas phase)	93.1	92.9	95.1	92.8

results of all four codes. In this context, it is also instructive to compare the results to ARD-B1. In doing so, it becomes evident that all codes are successful in describing the attenuation of Fe(II) release due to the formation of secondary minerals in a similar fashion.

5.3 Benchmark ARD-B3

Results for the third benchmark ARD-B3 are similar in nature to those obtained for ARD-B2 (compare Figs. 6 and 5). However, additional acid neutralization is provided by the

Fig. 6 Simulated profiles after 10 years for benchmark level III: **a** pH and pE; **b** mineral volume fractions; **c** total aqueous component concentrations of Fe(II), Fe(III), and SO$_4$; **d** pO$_2$ and pCO$_2$—*solid lines*: MIN3P, *dashed lines*: HP1, *dot-dashed lines*: Flotran, *dotted lines*: CrunchFlow
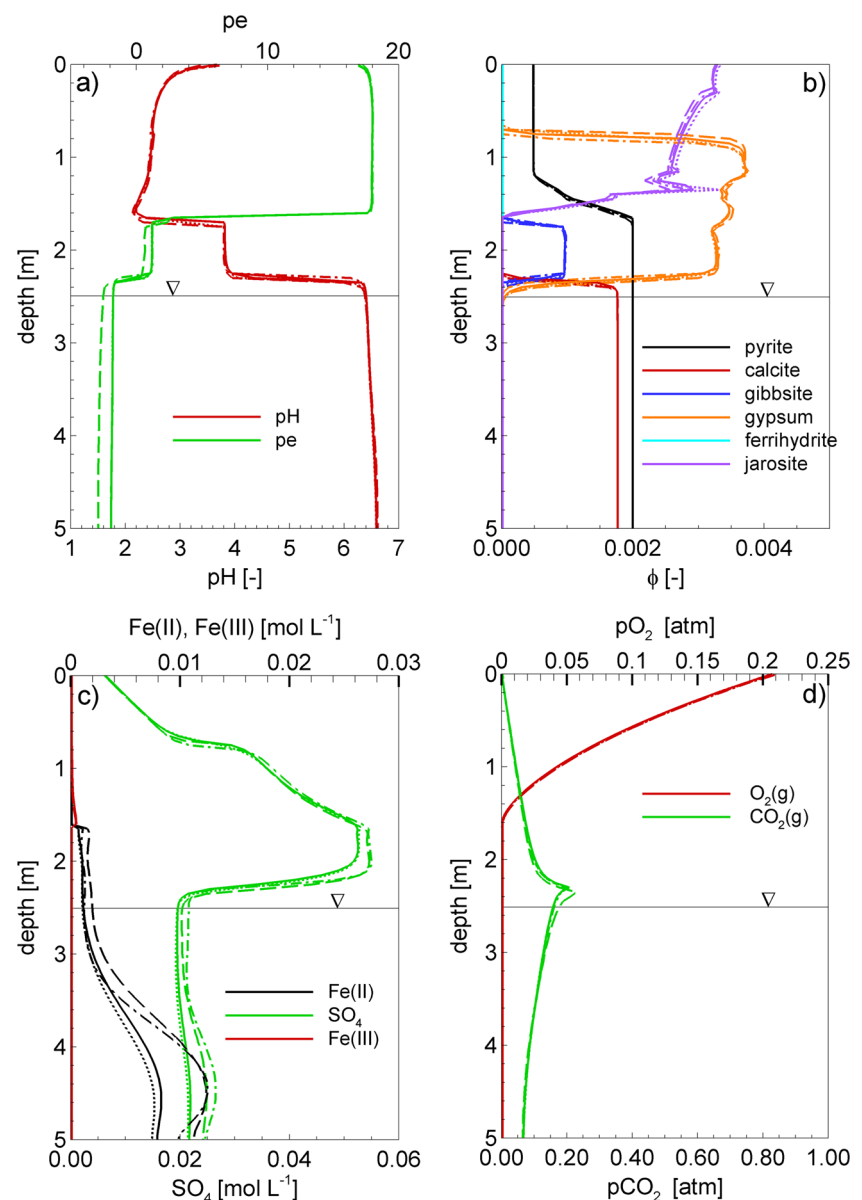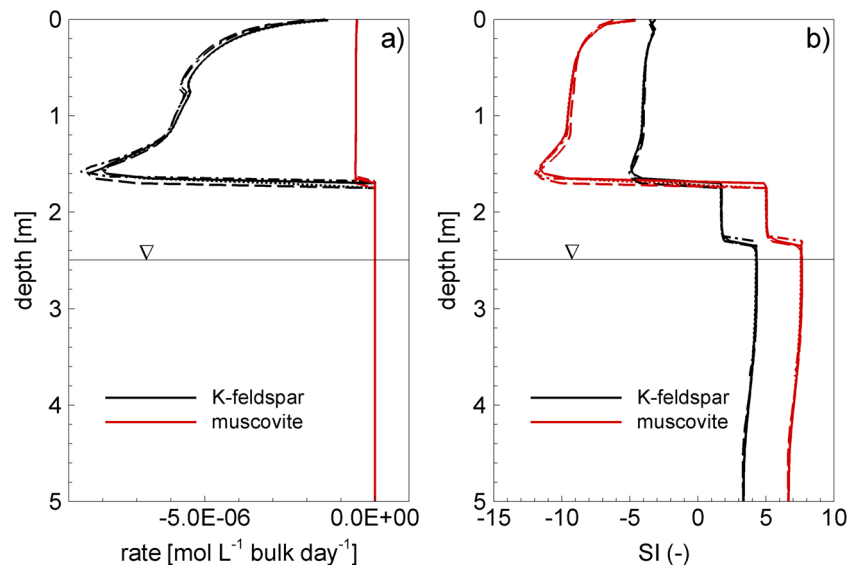
Fig. 7 Simulated profiles after 10 years for benchmark ARD-B3: **a** dissolution rates for K-feldspar and muscovite and **b** saturation indices for K-feldspar and muscovite—*solid lines*: MIN3P, *dashed lines*: HP1, *dot-dashed lines*: Flotran, *dotted lines*: CrunchFlow

dissolution of the silicate mineral phases, which leads to a slower downward migration of the calcite dissolution front. In addition, precipitation of gibbsite occurs, amorphous silica also precipitates, while ferrihydrite is not present in the

solution domain after $T = 10$ years. Increased jarosite precipitation occurs at the expense of ferrihydrite precipitation due to the release of K^+ from K-feldspar. In relation to ARD-B2, this leads to more acidic conditions in the upper vadose zone,

Fig. 8 Breakthrough curves for Fe(II) and SO_4 for benchmark ARD-B3 at $z = 2.5$ m, *solid lines*: MIN3P, *dashed lines*: HP1, *dot-dashed lines*: Flotran, *dotted lines*: CrunchFlow
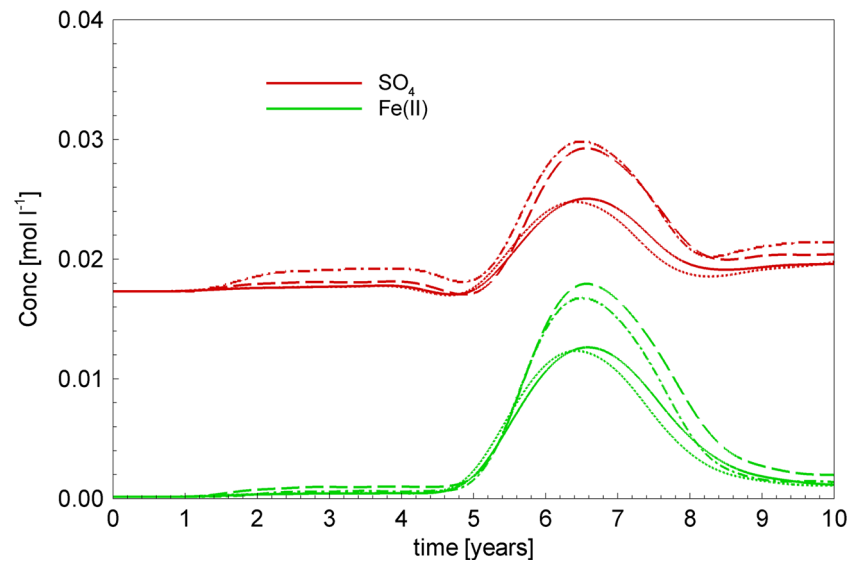
Table 6 Cumulative oxygen ingress, cumulative SO_4 and Fe(II) release after 10 years—benchmark ARD-B3

Mass ingress/release/egress [mol]	CrunchFlow	Flotran	HP1	MIN3P
$O_2(g)$ ingress	344.3	345.8	350.0	343.5
SO_4 release	53.6	53.9	54.6	53.9
Fe(II) release	3.6	3.3	4.9	3.8
$CO_2(g)$ egress (gas phase)	85.0	84.6	87.2	84.5

despite the increased pH buffering capacity. Supersaturated conditions are observed for the silicates in areas where calcite is still present (Fig. 7).

The agreement between the different codes is excellent for pH, pE, mineral assemblage, O_2 and CO_2 partial pressures (Fig. 6), silicate dissolution rates, and saturation indices (Fig. 7). However, more significant differences are seen for Fe(II) and SO_4 near the bottom of the domain (Fig. 6). While results from CrunchFlow and MIN3P agree well, higher concentrations are predicted by both Flotran and HP1. To assess the discrepancies in more detail, Fig. 8 depicts the breakthrough of Fe and SO_4 in the center of the domain directly below the water table ($z=2.5$ m). These results show that the maximum concentrations obtained by Flotran and HP1 are higher than those simulated by CrunchFlow and MIN3P; however, the time period of elevated concentration release is relatively short-lived, with limited effects on the mass balance. As for the previous benchmark levels, it is difficult to pinpoint the exact reasons for the observed differences. Analogous to ARD-B2, Table 6 compares the cumulative mass loadings predicted by the codes for the ingress of O_2, egress of CO_2, and release for Fe(II) and SO_4 at the base of the domain. The agreement of results between the four codes is very good for all parameters, with some larger differences for Fe(II), amplified by the fact that Fe(II) release at the discharge point represents a small fraction of Fe(II) release from pyrite oxidation, as discussed above. Model input parameters including boundary conditions, initial conditions, reactions stoichiometries, thermodynamic constants, rate coefficients, and parameters for activity corrections are provided in tabulated form. In addition, input and database files, as well as selected output files for the four participating codes CrucnchFlow, Flotran, HP1 and MIN3P are provided as either text files or Excel files.

6 Conclusions

A three-level benchmark problem was designed to provide an opportunity for intercomparison between reactive transport codes for problems involving mass transport in partially saturated porous media, including diffusive gas transport. The benchmark focuses on the generation and attenuation of acid rock drainage in a one-dimensional vertical profile of a hypothetical tailings impoundment constrained by parameters derived from previous simulations at field sites. The benchmark includes the most important mass transport and geochemical processes controlling water chemistry at mine waste sites, in particular mine tailings. Four reactive transport codes participated in the exercise (namely CrunchFlow, Flotran, HP1, and MIN3P), and overall excellent agreement was obtained between the various simulations. However, some discrepancies were observed for the breakthrough of Fe and SO_4 at the base of the domain. It is difficult to determine the exact reasons for

these residual differences; however, it is not uncommon that a perfect match between results cannot be obtained when benchmarking systems with a high level of process complexity. This is not restricted to the benchmarking of reactive transport codes, and has been seen in previous benchmark efforts focusing on other fields of study (e.g., carbon sequestration [7]). Nevertheless, despite small deviations in the results, it can be said with certainty that all four codes captured the geochemical and mineralogical evolution in a nearly identical fashion. Throughout the simulation, the same mineral assemblages, locations of the mineral dissolution fronts, and pH buffer regions were obtained. Cumulative mass balance loadings were also in close agreement. These results provide confidence in the use of multicomponent reactive transport codes for the assessment of laboratory experiments and field sites involving ARD problems. The results show that small differences obtained due to different implementations of the governing equations will not significantly affect the interpretation of the model results. Although these results are problem-specific, it is expected that computer codes passing this benchmark will be applicable to solve similar problems of the same type, meaning other one-dimensional ARD problems subject to different recharge rates, moisture distributions, mineralogy, and geochemical reactions. These results imply that when applying any of these models individually for history matching of data or in a predictive mode, uncertainties will be dominated by the conceptual model, and not by the implementation of the governing equations into the codes.

Conflict of interest The authors declare that they have no conflicts of interest.

References

1. Acero, P., Ayora, C., Carrera, J., Saaltink, M.W., Olivella, S.: Multiphase flow and reactive transport model in vadose tailings. Appl Geochem **24**, 1238–1250 (2009)

2. Allison, J. D., Brown, D.S., Novo-Gradac, K.J.: MINTEQA2/PRODEFA2, A geochemical assessment model for environmental systems, version 3.0, user's manual, EPA/600/3-91/021, Environ. Res. Lab., U.S. Environ. Prot. Agency, Washington, D. C. (1991)

3. Bea, S. A., Wilson, S. A., Mayer, K.U., Dipple, G. M., Power, I. M., Gamazo P.: Reactive transport modeling of natural carbon sequestration in ultramafic mine tailings, Vadose Zone J., 11, doi: 10.2136/vzj2011.0053 (2012)

4. Binning, P.J., Postma, D., Russell, T.F., Wesselingh, J.A., Boulin, P.F.: Advective and diffusive contributions to reactive gas transport during pyrite oxidation in the unsaturated zone. Water Resour Res **43**, W02414 (2007). doi:10.1029/2005WR004474

5. Blum A. E., Stillings, L. L.: Feldspar dissolution kinetics, Ch, 7 in Chemical weathering of silicate minerals, Rev. Mineral, Vol 31, Eds.: A. F. White & S. L. Brantley (1995)

6. Cathles, L.M.: Predictive capabilities of a finite difference model of copper leaching in low grade industrial sulfide waste dumps. Math Geol **11**, 175–191 (1979)

7. Class, H., Ebigbo, A., Helmig, R., Dahle, H.K., Nordbotten, J.M., Celia, M.A., Audigane, P., Darcis, M., Ennis-King, J., Fan, Y., Flemisch, B., Gasda, S.E., Jin, M., Krug, S., Labregere, D., Naderi Beni, A., Pawar, R.J., Sbai, A., Thomas, S.G., Trenty, L., Wei, L.: A benchmark study on problems related to CO$_2$ storage in geologic formations. Comput Geosci **13**, 409–434 (2009)

8. Demers, I., Molson, J., Bussiere, B., Laflamme, D.: Numerical modeling of contaminated neutral drainage from a waste-rock field test cell. Appl Geochem **33**, 346–356 (2013)

9. INAP, The global acid rock drainage guide, http://www.gardguide.com/index.php/Chapter_1, accessed, July 29, 2014

10. Jacques, D., Simunek, J., Mallants, D., van Genuchten, M.T.: Modelling coupled water flow, solute transport and geochemical reactions affecting heavy metal migration in a podzol soil. Geoderma **145**, 449–461 (2008)

11. Jaynes, D.B., Rogowski, A.S.S., Pionke, H.B.: Acid mine drainage from reclaimed coal strip mines. 1. Model description. Water Resour Res **20**, 233–242 (1984)

12. Lasaga, A.C.: Kinetic theory in the earth sciences. Princeton Univ. Press, Princeton, N. J (1998)

13. Lefebvre, R., Hockley, D., Smolensky, J., Gelinas, P.: Multiphase transfer processes in waste rock piles producing acid mine drainage 1: conceptual model and system characterization. J Contam Hydrol **52**, 137–164 (2001)

14. Lichtner, P.C.: Continuum formulation of multi-component multi-phase reactive transport. Ch. 1. In: Lichtner, P.C., Steefel, C.I., Oelkers, E.H. (eds.) Reactive transport in porous media, vol. 34. Mineralogical Society of America, Washington (1996). **Rev. Mineral**

15. Lichtner, P.C.: Modeling of reactive flow and transport in natural systems, in: Proceedings of the Rome seminar on environmental geochemistry, pp. 5–72, Castelnuovo di Porto, May 22–26 (1996)

16. Lichtner, P.C.: FLOTRAN user's manual: two-phase non-isothermal coupled thermal-hydrologic-chemical (THC) reactive flow and transport code, version 2. Los Alamos National Laboratory, Los Alamos, New Mexico (2007)

17. Linklater, C.M., Sinclair, D.J., Brown, P.L.: Coupled chemistry and transport modelling of sulphidic waste rock dumps at the Aitik mine site, Sweden. Appl Geochem **20**, 275–293 (2005)

18. Mayer, K. U., Blowes D. W., Frind, E. O.: Numerical modeling of acid mine drainage generation and subsequent reactive transport. ICARD 2000, Proceedings from the fifth international Conference on acid rock drainage, sponsored by the Society of Economic Geologists, Denver, Colorado, May 21–24,Vol. 1, 135–142 (2000)

19. Mayer, K.U., Frind, E.O., Blowes, D.W.: Multicomponent reactive transport modeling in variably saturated porous media using a generalized formulation for kinetically controlled reactions. Water Resour Res **38**, 1174 (2002). doi:10.1029/2001WR000862

20. Mayer, K.U., MacQuarrie, K.T.B.: Solution of the MoMaS reactive transport benchmark with MIN3P - model formulation and simulation results. Comput Geosci **14**, 405–419 (2010)

21. Molins, S., Mayer, K.U.: Coupling between geochemical reactions and multicomponent gas diffusion and advection – a reactive transport modeling study. Water Resour Res **43**, W05435 (2007). doi:10.1029/2006WR005206

22. Molson, J.W., Fala, O., Aubertin, M., Bussiere, B.: Numerical simulations of pyrite oxidation and acid mine drainage in unsaturated waste rock piles. J Contam Hydrol **78**, 343–371 (2005)

23. Millington, R.J.: Gas diffusion in porous media. Science **130**, 100–102 (1959)

24. Nagy, K.L.: Dissolution and precipitation kinetics of sheet silicates, Ch, 5 in Chemical weathering of silicate minerals, Rev. Mineral, Vol 31, Eds.: A. F. White & S. L. Brantley (1995)

25. Neuman, S.P.: Saturated-unsaturated seepage by finite elements. J Hydrol Div Am Soc Civ Eng **99**(HY12), 2233–2250 (1973)

26. Nordstrom, D.K., Alpers, C.N., Ptacek, C.J., Blowes, D.W.: Negative pH and extremely acidic mine waters from Iron Mountain, California. Environ Sci Technol **34**, 254–258 (2000)

27. Panday, S., Huyakorn, P.S., Therrien, R., Nichols, R.L.: Improved three-dimensional finite-element techniques for field simulation of variably-saturated flow and transport. J Contam Hydrol **12**, 3–33 (1993)

28. Steefel, C.I., Lasaga, A.C.: A coupled model for transport of multiple chemical species and kinetic precipitation/dissolution reactions with application to reactive flow in single phase hydrothermal systems. Am J Sci **294**, 529–592 (1994)

29. Steefel, C.I., Appelo, C.A.J., Hammond, G., Kolditz, O., Lagneau, V., Lichtner, P.C., Mayer, K.U., Meussen, H., Molins, S., Parkhurst, D.L., Shao, H., Sonnenthal, E.L., Spycher, N., Van der Lee, J., Yabusaki, S.B., Yeh, G.-T.: Subsurface environmental simulation benchmarks: formulation and code descriptions. Comput Geosci (2015). doi:10.1007/s10596-014-9443-x

30. Van Genuchten, M.T.: A closed form equation for predicting the hydraulic conductivity of unsaturated soils. Soil Sci Soc Am J **44**, 892–898 (1980)

31. Yeh, G.T., Tripathi, V.S.: A critical evaluation of recent developments in hydrogeochemical transport models of reactive multi-chemical components. Water Resour Res **25**, 93–108 (1989)

32. Walter, A.L., Frind, E.O., Blowes, D.W., Ptacek, C.J., Molson, J.W.: Modelling of multicomponent reactive transport in groundwater, 1. Model development and evaluation. Water Resour Res **30**, 3137–3148 (1994)

33. Walter, A.L., Frind, E.O., Blowes, D.W., Ptacek, C.J., Molson, J.W.: Modelling of multicomponent reactive transport in groundwater, 2. Metal mobility in aquifers impacted by acidic mine tailings discharge. Water Resour Res **30**, 3149–3158 (1994)

34. Wunderly, M.D., Blowes, D.W., Frind, E.O., Ptacek, C.J.: Sulfide mineral oxidation and subsequent reactive transport of oxidation products in mine tailings impoundments: a numerical model. Water Resour Res **32**, 3173–3187 (1996)

35. Xu, T.F., Pruess, K.: Modeling multiphase non-isothermal fluid flow and reactive geochemical transport in variably saturated fractured rocks: 1. Methodology. Am J Sci **301**, 16–33 (2001)

36. Yabusaki, S.B., Fang, Y., Williams, K.H., Murray, C.J., Ward, A.L., Dayvault, R.D., Waichler, S.R., Newcomer, D.R., Spane, F.A., Long, P.E.: Variably saturated flow and multicomponent biogeochemical reactive transport modeling of a uranium bioremediation field experiment. J Contam Hydrol **126**, 271–290 (2011)